Scientia Iranica B (2022) 29(2), 597–611

Sharif University of Technology
Scientia Iranica
Transactions B: Mechanical Engineering
http://scientiairanica.sharif.edu

Research Note

Attitude control of a spacecraft during an orbital maneuver for fast rejection of large disturbance torque without using the reaction control system

H. Kouhi*

Department of Mechanical Engineering, University of Guilan, Rasht, P.O. Box 4199613776, Iran.

Received 21 August 2020; received in revised form 6 May 2021; accepted 28 August 2021

KEYWORDS
Impulsive orbital maneuver;
Large disturbance rejection;
Fast disturbance rejection;
Control moment gyro;
Reaction control system.

Abstract. During an impulsive orbital maneuver, thrust vector misalignment from the Center of Mass (CM) generates a large exogenous disturbance torque that results in attitude deviation. This paper aims to eliminate the need for application of Reaction Control System (RCS) for spacecraft attitude control. In order to reject large disturbance very fast, a new control system is proposed. In this method, the large disturbance torque is rejected quickly without using RCS. The control system is based on one Degree of Freedom (1DoF) gimbaled-thruster, spin-stabilization, and two Control Moment Gyros (CMG). The nonlinear two-body dynamics of the mentioned spacecraft is formulated. Given that RCS is not used, this method is an efficient and implementable one for attitude control of a small spacecraft. Numerical simulation shows that thrust vector deviation converges to zero despite disturbance torques. Through this method, the disturbance is rejected very fast, hence an accurate orbital velocity change can be obtained. This method can eliminate the initial attitude deviation easily and overcome disturbance rejection. The results exhibited the good performance and superiority of the proposed method compared to some other thrusting maneuver methods.

1. Introduction

The important role of spacecraft attitude control in the impulsive orbital maneuver has been discussed in a number of studies [1,2]. Thrust vector offset from the Center of Mass (CM) is always observed during an orbital maneuver [2]. This misalignment produces a large disturbance torque that results in thrust vector deviation from the desired inertial direction [3]. A spacecraft needs a powerful attitude control system to reject the mentioned large exogenous disturbance quickly.

*. *Tel.: +98-1333690274-6087*
E-mail address: hamed.koohi@guilan.ac.ir

doi: 10.24200/sci.2021.56648.4835

In order to compensate for the disturbance from the orbital engine, an identification algorithm was proposed in [2] to estimate the position of CM and a hybrid controller based on momentum actuators (like Control Moment Gyros (CMG)) and thrusters was proposed for attitude control and rejection of the disturbance. Several types of researches have addressed the non-impulsive orbital maneuver; see [4,5]. During a non-impulsive orbital maneuver, the disturbance level is quite low, hence no need for a large attitude control torque. In addition to the attitude control methods presented in [6], another method was introduced in [7] that functioned based on a one Degree of Freedom (1DoF) gimbaled-thruster, spin-stabilization, and two Reaction Wheels (RW).

A simple and reliable attitude control scheme is

spin stabilization [8]. The spin stabilization (without Reaction Control System (RCS) and Thrust Vector Control (TVC) used only in many space projects is subject to some disadvantages and limitations. For a spacecraft spinning around its axis of minimum moment of inertia, the attitude (thrust vector) is unstable (occurring nutational or coning instability). Thus, an RCS (with fuel consumption) is needed for nutation control [9]. If the spin axis (thrust vector direction) deviates from the desired inertial direction, an active control system (e.g., RCSs) should be employed to stabilize the thrust direction [10]. Moreover, only spin stabilization method fails to eliminate the initial attitude deviation (before the firing).

Given that the RCSs can provide a large control torque, they perform attitude maneuvers and reject exogenous disturbances [11]. However, in practice, they have some drawbacks and requirements that make them inappropriate for application in small spacecraft. Their application to small spacecrafts is not recommended because it includes many complex components and fuel tanks. In the presence of fuel sloshing, attitude control of a spacecraft is quite difficult [12]. RCSs exhibit nonlinear behavior and hence, need complex control logic [13]. Although a combination of RCSs and TVC is a large spacecraft (see [14,15]), RCSs alone are not suitable in a small spacecraft mission; therefore, small spacecraft need a new control system, especially for rejecting large disturbance torques.

TVC method is a powerful technique for controlling spacecraft and launchers [16] with no fuel consumption. The control torque of a TVC can be larger than the disturbance caused by the thrust vector misalignment. In addition, it can be a support for the attitude control system [17]. The thrust vector misalignment can be eliminated using the TVC [18]. The applicability and other advantages of the TVC method are addressed in [15,19]. In a small spacecraft, a 1DoF TVC preferred to a 2DoF TVC due to structural requirements. While some studies such as [15] employed a 2DoF TVC and eight RCSs (full actuated) to eliminate thrust vector misalignment, the present study used a 1DoF TVC for the same purpose. In contrast to many types of research, the current study investigated how to control an underactuated system.

This research aims to reject the large disturbance torque as fast as possible with no need for using RCS. The proposed method is efficient for small spacecrafts because using the RCS is not suitable for small ones. As seen in the previous works (except [7]), disturbance rejection and thrust vector stabilization are not possible during an orbital maneuver without the RCS. Of note, in case the level of disturbance is high, the method used in [7] was not applicable.

Since momentum exchange devices (such as RWs and CMGs) do not consume fuel propellants, they gained popularity in attitude control [20]. Attitude control systems based on only these actuators cannot reject the external disturbances. Consequently, these actuators cannot be used alone in a thrusting maneuver. A small torque can be produced through the interaction between the spacecraft spin rate and angular momentum of RWs by which the exogenous disturbance torque can be rejected during the Solid Rocket Motor (SRM) burning [7].

The objective of this paper is fast disturbance rejection and thrust vector stabilization without using the RCS considering a large disturbance torque. Despite the several advantages illustrated by the study [7] such as simplicity, full disturbance rejection, and thrust vector stabilization, the proposed method has some limitations. Since each RW rotation axis is fixed to the body, its angular momentum interacts with the spinning rate of the spacecraft and the gyroscopic torque deviates from the attitude. This is the reason why its angular momentum must be zero before firing (before firing, the TVC cannot operate) and RWs must be activated during burning (TVC is on). On the contrary, the burning time is short and the RW axial torque is not large enough to quickly generate a large angular momentum. This condition is not desirable because the disturbance torque must be rejected very fast. Small RWs in this method are not applicable and large disturbance torques cannot be rejected. In addition, the RW [7] is subject to another drawback, that is, disturbance rejection is undesirably slow.

The current research proposes a new attitude control system based on spin stabilization, a 1DoF gimbaled-thruster, and two single-gimbal CMGs. CMG plays an important role in attitude control of large spacecrafts due to its powerful momentum storage capacity and astonishing torque amplification ability [21,22]. Two momentum wheels that are gimbaled on the spacecraft body work as two CMGs. In this method, two large angular momentums can be produced before firing because they do not interact with the spinning rate of the spacecraft. Therefore, there is enough time to generate large angular momentum through which a large control torque can be obtained during firing. In other words, the large disturbance torque can be rejected using two small CMGs. Since two CMGs are gimbaled on the spacecraft body, the disturbance rejection can be completed very fast due to the quick changes in angular momentum direction. This method can be applied to small spacecrafts owing to the application of small CMGs with a high-level angular momentum. One of the objectives of this study was to reject the disturbance. To this end, similar to [23], a nonlinear disturbance observer was utilized to estimate the disturbance level. Although the linearized model was used for controller design, the linear controller in all simulations was applied to the nonlinear

system to confirm the applicability of the proposed method [24]. In other words, the closed-loop system includes a linear controller and a nonlinear plant.

The paper is organized as follows: Section 2 illustrates the spacecraft dynamic modeling. Section 3 introduces control logic including the TVC logic and CMG steering logic. Section 4 lists the spacecraft parameters. Section 5 designs the parameters of the closed-loop control system. Section 6 presents numerical simulation results. Finally, Section 7 concludes this study.

2. Dynamic modeling

2.1. Nonlinear dynamic modeling

Figure 1 shows the main parts of the spacecraft. There is a spin rate $\overline{\omega}_s$ about its longitudinal axis in this spin-stabilized spacecraft.

The free-body diagram of the spacecraft equipped with two CMGs is depicted in Figure 2. The nozzle can rotate along the axis $x_s(x_n)$ using a 1DoF gimbal actuator at the pivot o. In this figure, the point of the thrust force, gimbal pivot, body, and nozzle are denoted by subscripts T, o, s, and n, respectively; G_s and G_n show the CM locations of the body and nozzle, respectively; $\boldsymbol{\tau}_s$ and $\boldsymbol{\omega}_s$ represent the body exogenous torque and angular velocity, respectively; $\mathbf{M}_o$ and $\mathbf{F}_o$ are the internal torque and force in the pivot o; and $\boldsymbol{\tau}_n$ and $\boldsymbol{\omega}_n$ are the nozzle torque and angular velocity, respectively. In Figure 3, β denotes the thruster angle around the axis x_s. Note that prior to firing, the rotation axis of each wheel of the CMG is parallel to the z_s axis.

In Figure 4, the direction of the two wheels is shown where w_1 and w_2 represent the first and second wheels, respectively. Figure 5 shows the structural details of two CMGs. Before the thrusting maneuver, two wheels have equal angular momentum h_w, but in opposite directions. Angles γ_x (around x_s) and γ_y (around y_s) show the gimbal angles of w_1 and w_2, respectively. Figures 6 and 7 depict the rotation of two angular momentums around y_s and x_s, respectively. These two angles are the control inputs of the two CMGs used during the disturbance rejection. Given that $\gamma_x = 0$ and $\gamma_y = 0$ before the thrusting maneuver, the resultant angular momentum is zero $(h_w - h_w = 0)$, hence it does not affect the spacecraft attitude. Therefore, the value of h_w can reach its maximum value. Before a thrusting maneuver, there is enough time to generate a large h_w using electrical power. In other words, before thrusting maneuver,

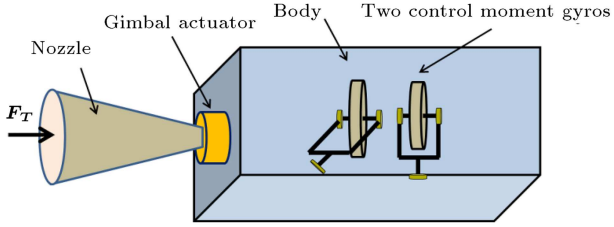

Figure 1. Spacecraft equipped with a gimbaled-nozzle and two CMGs.

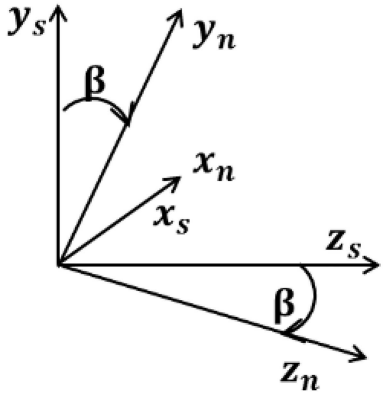

Figure 3. The rotation angle of the gimbal actuator at the pivot o.

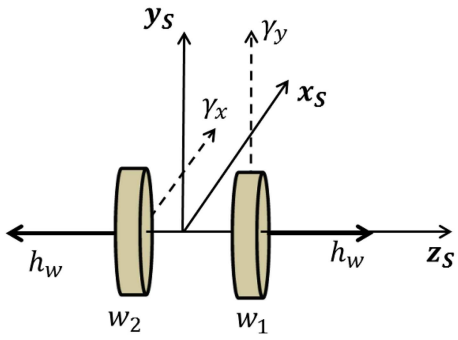

Figure 4. Two CMGs with gimbal angles γ_x and γ_y.

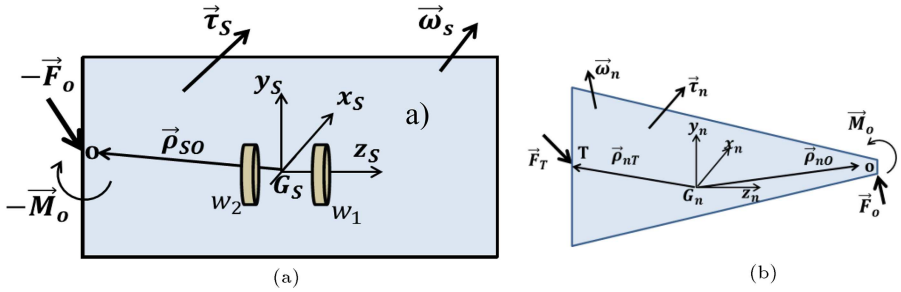

(a) (b)

Figure 2. Spacecraft body (a) and thruster (b) with two CMGs at G_s.

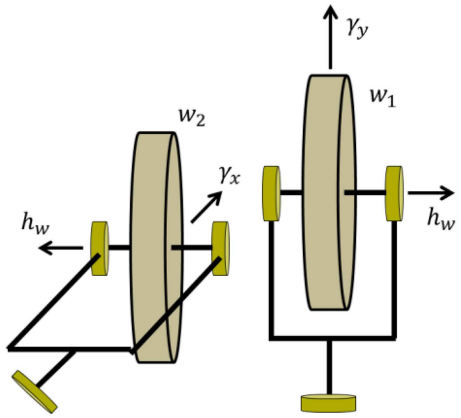

Figure 5. The details of two CMGs' structures.

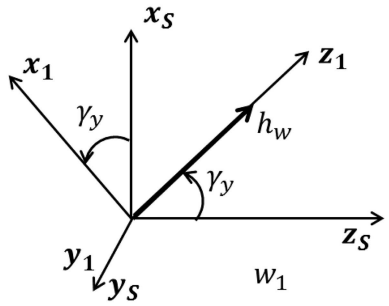

Figure 6. Rotation of the angular momentum of wheel 1 around the y_s.

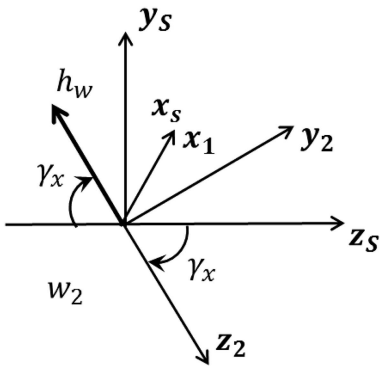

Figure 7. Rotation of the angular momentum of wheel 2 around the x_s.

both h_w and spacecraft spin rate ($\overline{\omega}_s$) can increase simultaneously. During the thrusting maneuver, the value of h_w remains constant and two angles γ_x and γ_y are controlled to reject the disturbance torques.

Figure 8 elaborates how two wheels can be used as two RWs along the two axes x_s and y_s. When a spacecraft is not at the thrusting maneuver phase, two angles can be set to $\gamma_x = 90°$ and $\gamma_y = 90°$, thus achieving two RWs that can be used for attitude control of the spacecraft during non-thrusting phases. This can be regarded as another advantage of the proposed method.

The angular momentums of two CMGs with

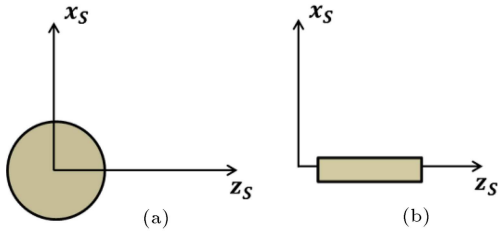

Figure 8. Application of two CMGs as two RWs.

respect to the inertial reference frame are as follows:

$$\mathbf{H}_1 = \mathbf{I}_1^s \boldsymbol{\omega}_s + \mathbf{h}_1^s,$$

$$\mathbf{H}_2 = \mathbf{I}_2^s \boldsymbol{\omega}_s + \mathbf{h}_2^s, \tag{1}$$

where:

$$\mathbf{h}_1^s = h_w \begin{bmatrix} \sin(\gamma_y) & 0 & \cos(\gamma_y) \end{bmatrix}^T + \frac{J_d}{2}\dot{\gamma}_y \begin{bmatrix} 0 & 1 & 0 \end{bmatrix}^T,$$

$$\mathbf{h}_2^s = h_w \begin{bmatrix} 0 & \sin(\gamma_x) & -\cos(\gamma_x) \end{bmatrix}^T + \frac{J_d}{2}\dot{\gamma}_x \begin{bmatrix} 1 & 0 & 0 \end{bmatrix}^T,$$

$$\mathbf{I}_1^s = \left[\mathbf{R}_s^1\right]^T \mathbf{I}_w^1 \mathbf{R}_s^1, \qquad \mathbf{I}_2^s = \left[\mathbf{R}_s^2\right]^T \mathbf{I}_w^2 \mathbf{R}_s^2,$$

$$\mathbf{I}_w^1 = \mathbf{I}_w^2 = J_d \begin{bmatrix} 0.5 & 0 & 0 \\ 0 & 0.5 & 0 \\ 0 & 0 & 1 \end{bmatrix},$$

$$\mathbf{R}_s^1 = \begin{bmatrix} \cos(\gamma_y) & 0 & -\sin(\gamma_y) \\ 0 & 1 & 0 \\ \sin(\gamma_y) & 0 & \cos(\gamma_y) \end{bmatrix},$$

$$\mathbf{R}_s^2 = \begin{bmatrix} 1 & 0 & 0 \\ 0 & \cos(\gamma_x) & \sin(\gamma_x) \\ 0 & -\sin(\gamma_x) & \cos(\gamma_x) \end{bmatrix}.$$

The angular momentum of each wheel is calculated through $h_w = J_d \omega_g$, where J_d and ω_g are the axial moment of inertia and spin of the wheel, respectively.

According to Euler momentum equation, the time derivative of Eq. (1) results in the moments, as shown in the following:

$$\boldsymbol{\tau}_1^s = \mathbf{I}_1^s \dot{\boldsymbol{\omega}}_s + \boldsymbol{\omega}_s \times (\mathbf{I}_1^s \boldsymbol{\omega}_s) + \boldsymbol{\omega}_s \times \mathbf{h}_1^s + \dot{\mathbf{h}}_1^s, \tag{2}$$

$$\boldsymbol{\tau}_2^s = \mathbf{I}_2^s \dot{\boldsymbol{\omega}}_s + \boldsymbol{\omega}_s \times (\mathbf{I}_2^s \boldsymbol{\omega}_s) + \boldsymbol{\omega}_s \times \mathbf{h}_2^s + \dot{\mathbf{h}}_2^s, \tag{3}$$

where:

$$\dot{\mathbf{h}}_1^s = h_w \dot{\gamma}_y \begin{bmatrix} \cos(\gamma_y) & 0 & -\sin(\gamma_y) \end{bmatrix}^T + \frac{J_d}{2}\ddot{\gamma}_y \begin{bmatrix} 0 & 1 & 0 \end{bmatrix}^T,$$

and:

$$\dot{\mathbf{h}}_2^s = h_w \dot{\gamma}_x \begin{bmatrix} 0 & \cos(\gamma_x) & \sin(\gamma_x) \end{bmatrix}^T + \frac{J_d}{2}\ddot{\gamma}_x \begin{bmatrix} 1 & 0 & 0 \end{bmatrix}^T.$$

Note that while $\boldsymbol{\tau}_1^s$ and $\boldsymbol{\tau}_2^s$ are applied to the CMGs, the

reactions $-\boldsymbol{\tau}_1^s$ and $-\boldsymbol{\tau}_2^s$ are used in the spacecraft body. The superscript s indicates that a vector is expressed in the spacecraft body coordinate frame.

The Euler momentum equation for the body is:

$$\boldsymbol{\tau}_s-\boldsymbol{\tau}_1^s-\boldsymbol{\tau}_2^s-\boldsymbol{\rho}_{so}\times\mathbf{F}_o-\mathbf{M}_o=\mathbf{I}_{s,0}\dot{\boldsymbol{\omega}}_s+\boldsymbol{\omega}_s\times(\mathbf{I}_{s,o}\boldsymbol{\omega}_s), \tag{4}$$

where $\mathbf{I}_{s,0}$ is the spacecraft body moment of inertia.

Following the summation of Eqs. (2)–(4), we have:

$$\boldsymbol{\tau}_s-\boldsymbol{\tau}_{CMG}-\boldsymbol{\rho}_{so}\times\mathbf{F}_o-\mathbf{M}_o=\mathbf{I}_s\dot{\boldsymbol{\omega}}_s+\boldsymbol{\omega}_s\times(\mathbf{I}_s\boldsymbol{\omega}_s), \tag{5}$$

where:

$$\boldsymbol{\tau}_{CMG}=\boldsymbol{\omega}_s\times(\mathbf{h}_1^s+\mathbf{h}_2^s)+(\dot{\mathbf{h}}_1^s+\dot{\mathbf{h}}_2^s),$$

and:

$$\mathbf{I}_s=\mathbf{I}_{s,0}+\mathbf{I}_1^s+\mathbf{I}_2^s.$$

Euler momentum equation of the nozzle in its coordinate frame is as follows:

$$\boldsymbol{\tau}_n^n+\boldsymbol{\rho}_{no}^n\times\mathbf{F}_o^n+\mathbf{M}_o^n+\boldsymbol{\rho}_{nT}^n\times\mathbf{F}_T^n=\mathbf{I}_n^n\dot{\boldsymbol{\omega}}_n^n+\boldsymbol{\omega}_n^n\times(\mathbf{I}_n^n\boldsymbol{\omega}_n^n). \tag{6}$$

The superscript n is used to describe a vector in the nozzle coordinate frame (the superscript s is not shown in equations). Here, $\mathbf{I}_n^n$ is the nozzle moment of inertia in its coordinate frame.

For the summation of Eqs. (5) and (6), they must be expressed in the same coordinate frame and the rotation matrix between the body and nozzle frame is defined as follows:

$$\mathbf{R}_n^s(\beta)=\begin{bmatrix}1 & 0 & 0\\ 0 & \cos(\beta) & -\sin(\beta)\\ 0 & \sin(\beta) & \cos(\beta)\end{bmatrix}. \tag{7}$$

Based on the transformations in Eq. (8), Eq. (6) is reformed into Eq. (9):

$$\begin{aligned}
&\boldsymbol{\tau}_n=\mathbf{R}_n^s\boldsymbol{\tau}_n^n, \qquad \mathbf{M}_o=\mathbf{R}_n^s\mathbf{M}_o^n, \qquad \mathbf{I}_n=\mathbf{R}_n^s\mathbf{I}_n^n\mathbf{R}_n^{sT},\\
&\boldsymbol{\rho}_{no}\times\mathbf{F}_o=\mathbf{R}_n^s(\boldsymbol{\rho}_{no}^n\times\mathbf{F}_o^n), \qquad \boldsymbol{\rho}_{no}=\mathbf{R}_n^s\boldsymbol{\rho}_{no}^n,\\
&\mathbf{F}_o=\mathbf{R}_n^s\mathbf{F}_o^n, \qquad \boldsymbol{\rho}_{nT}\times\mathbf{F}_T=\mathbf{R}_n^s(\boldsymbol{\rho}_{nT}^n\times\mathbf{F}_T^n),\\
&\boldsymbol{\rho}_{nT}=\mathbf{R}_n^s\boldsymbol{\rho}_{nT}^n, \qquad \mathbf{F}_T=\mathbf{R}_n^s\mathbf{F}_T^n.
\end{aligned} \tag{8}$$

$$\boldsymbol{\tau}_n+\boldsymbol{\rho}_{no}\times\mathbf{F}_o+\mathbf{M}_o+\boldsymbol{\rho}_{nT}\times\mathbf{F}_T=\mathbf{I}_n\dot{\boldsymbol{\omega}}_n+\boldsymbol{\omega}_n\times(\mathbf{I}_n\boldsymbol{\omega}_n). \tag{9}$$

The summation of Eqs. (9) and (5) gives:

$$\begin{aligned}
\boldsymbol{\tau}_{ns}-\boldsymbol{\tau}_{CMG}+\boldsymbol{\rho}_{ns}\times\mathbf{F}_o+\boldsymbol{\rho}_{nT}\times\mathbf{F}_T&=\mathbf{I}_{ns}\dot{\boldsymbol{\omega}}_s\\
&+\mathbf{I}_n(\dot{\boldsymbol{\omega}}_r+\boldsymbol{\omega}_s\times\boldsymbol{\omega}_r)+\boldsymbol{\omega}_s\times(\mathbf{I}_s\boldsymbol{\omega}_s)+\boldsymbol{\omega}_n\times(\mathbf{I}_n\boldsymbol{\omega}_n),
\end{aligned} \tag{10}$$

where:

$$\begin{aligned}
&\boldsymbol{\omega}_n=\boldsymbol{\omega}_s+\boldsymbol{\omega}_r, \qquad \dot{\boldsymbol{\omega}}_n=\dot{\boldsymbol{\omega}}_s+\dot{\boldsymbol{\omega}}_r+\boldsymbol{\omega}_s\times\boldsymbol{\omega}_r,\\
&\boldsymbol{\tau}_{ns}=\boldsymbol{\tau}_s+\boldsymbol{\tau}_n, \qquad \boldsymbol{\rho}_{ns}=\boldsymbol{\rho}_{no}-\boldsymbol{\rho}_{so},\\
&\boldsymbol{\rho}_{sn}=-\boldsymbol{\rho}_{ns}, \qquad \mathbf{I}_{ns}=\mathbf{I}_s+\mathbf{I}_n.
\end{aligned}$$

$\dot{\boldsymbol{\omega}}_r$ and $\boldsymbol{\omega}_r$ are the relative angular acceleration and velocity of the nozzle with respect to the body, respectively:

$$\boldsymbol{\omega}_r=\begin{bmatrix}\dot{\beta} & 0 & 0\end{bmatrix}^T, \qquad \dot{\boldsymbol{\omega}}_r=\begin{bmatrix}\ddot{\beta} & 0 & 0\end{bmatrix}^T. \tag{11}$$

In order to remove the unknown force $\mathbf{F}_o$ in Eq. (10), Newton's law and kinematic equations for both body and nozzle are obtained as follows:

$$\begin{cases}\mathbf{F}_T+\mathbf{F}_o=\mathbf{m}_n\mathbf{a}_{Gn}\\ -\mathbf{F}_o=\mathbf{m}_s\mathbf{a}_{Gs}\end{cases}$$

$$\begin{cases}\mathbf{a}_o=\mathbf{a}_{Gn}+\dot{\boldsymbol{\omega}}_n\times\boldsymbol{\rho}_{no}+\boldsymbol{\omega}_n\times(\boldsymbol{\omega}_n\times\boldsymbol{\rho}_{no})\\ \mathbf{a}_o=\mathbf{a}_{Gs}+\dot{\boldsymbol{\omega}}_s\times\boldsymbol{\rho}_{so}+\boldsymbol{\omega}_s\times(\boldsymbol{\omega}_s\times\boldsymbol{\rho}_{so})\end{cases} \tag{12}$$

that give $\mathbf{F}_o$ as:

$$\begin{aligned}
\mathbf{F}_o=&-\mathbf{F}_T(M/m_n)+M\,(\dot{\boldsymbol{\omega}}_s\times\boldsymbol{\rho}_{sn}-(\dot{\boldsymbol{\omega}}_r+\boldsymbol{\omega}_s\times\boldsymbol{\omega}_r)\\
&\times\boldsymbol{\rho}_{no}+\boldsymbol{\omega}_s\times(\boldsymbol{\omega}_s\times\boldsymbol{\rho}_{so})-\boldsymbol{\omega}_n\times(\boldsymbol{\omega}_n\times\boldsymbol{\rho}_{no})),
\end{aligned} \tag{13}$$

where m_s and m_n are the masses of the body and nozzle, respectively, and $M=(m_nm_s)/(m_n+m_s)$. By substituting Eq. (13) into Eq. (10), the angular acceleration of the spacecraft body is calculated as follows:

$$\dot{\boldsymbol{\omega}}_s=[\mathbf{I}_{ns,T}]^{-1}\,\mathbf{T}_s, \tag{14}$$

where:

$$\begin{aligned}
\mathbf{T}_s=&\boldsymbol{\tau}_{ns}-\boldsymbol{\tau}_{CMG}+\boldsymbol{\rho}_T\times\mathbf{F}_T-\mathbf{I}_r(\dot{\boldsymbol{\omega}}_r+\boldsymbol{\omega}_s\times\boldsymbol{\omega}_r)\\
&+M\boldsymbol{\rho}_{ns}\times(\boldsymbol{\omega}_s\times(\boldsymbol{\omega}_s\times\boldsymbol{\rho}_{so})-\boldsymbol{\omega}_n\times(\boldsymbol{\omega}_n\times\boldsymbol{\rho}_{no}))\\
&-\boldsymbol{\omega}_s\times(\mathbf{I}_s\boldsymbol{\omega}_s)-\boldsymbol{\omega}_n\times(\mathbf{I}_n\boldsymbol{\omega}_n),
\end{aligned}$$

and:

$$\begin{aligned}
&\mathbf{T}_s=\begin{bmatrix}T_x & T_y & T_z\end{bmatrix}^T, \qquad \boldsymbol{\omega}_s=\begin{bmatrix}\omega_{sx} & \omega_{sy} & \omega_{sz}\end{bmatrix}^T,\\
&\mathbf{I}_{ns,T}=\mathbf{I}_{ns}-M[\boldsymbol{\rho}_{ns}\times]^2, \qquad \mathbf{I}_r=\mathbf{I}_n-M[\boldsymbol{\rho}_{ns}\times][\boldsymbol{\rho}_{no}\times],\\
&\boldsymbol{\rho}_T=\boldsymbol{\rho}_{nT}+\boldsymbol{\rho}_{sn}(M/m_n).
\end{aligned}$$

Note that in Eq. (14), the control inputs are defined by $\boldsymbol{\tau}_{CMG}$ (for disturbance rejection) and $\ddot{\beta}$ (for gimbaled-TVC).

2.2. Spacecraft kinematics

According to [25], the Euler angles φ, θ, and ψ are used to describe the body orientation with respect to the inertial coordinate frame $X_I Y_I Z_I$. Their derivatives are:

$$\begin{bmatrix}\dot{\varphi} & \dot{\theta} & \dot{\psi}\end{bmatrix}^T = \mathbf{J}_{\omega}^{Eu}(\varphi,\theta,\psi)\boldsymbol{\omega}_s, \tag{15}$$

where:

$$\mathbf{J}_{\omega}^{Eu} = \begin{bmatrix}1 & \sin(\varphi)\tan(\theta) & \cos(\varphi)\tan(\theta)\\ 0 & \cos(\varphi) & -\sin(\varphi)\\ 0 & \sin(\varphi)/\cos(\theta) & \cos(\varphi)/\cos(\theta)\end{bmatrix}.$$

The desired velocity change and burning time that determine an orbital maneuver are Δv_d and T_b, respectively. The actual velocity change in the Z_I direction is:

$$\Delta v_z = \int_0^{T_b} a_{\max}\cos(\delta_{FT}(t))dt, \tag{16}$$

where:

$$\delta_{FT}(t) = \cos^{-1}(\cos(\theta(t))\cos(\varphi(t)+\beta(t))),$$

is the thrust vector deviation from the Z_I direction, and the maximum acceleration $a_{\max}$ and thrust F_T are calculated by:

$$a_{\max} = \Delta v_d/T_b, \qquad F_T = a_{\max}(m_s+m_n). \tag{17}$$

2.3. Disturbance model

The most important inputs that cause deviation in the spacecraft attitude are lateral disturbance torques (τ_{dx} and τ_{dy}), as shown in Figure 9, which are generated by thrust vector misalignment.

In Figure 9, $p_d(x_s, y_s)$ is the point of passing the thrust force for zero gimbal angle ($\beta = 0$), and x_s and y_s are the CM offset or thrust vector misalignment.

In the previous works such as [15,26], disturbances were supposed to be constant (due to the constant CM offset). The disturbance model is established based on the spacecraft dynamics (Eq. (14)), as shown below:

$$\tau_{dx} \approx (y_s F_T M)/m_n,$$

$$\tau_{dy} \approx -(x_s F_T M)/m_n. \tag{18}$$

In Figure 10, $p_g(x_s, y_s - \beta z_s)$ is the point of passing the thrust force for $\beta \neq 0$ and $\tau_g = -F_T z_s \beta$ is the control torque generated by gimbal deflection.

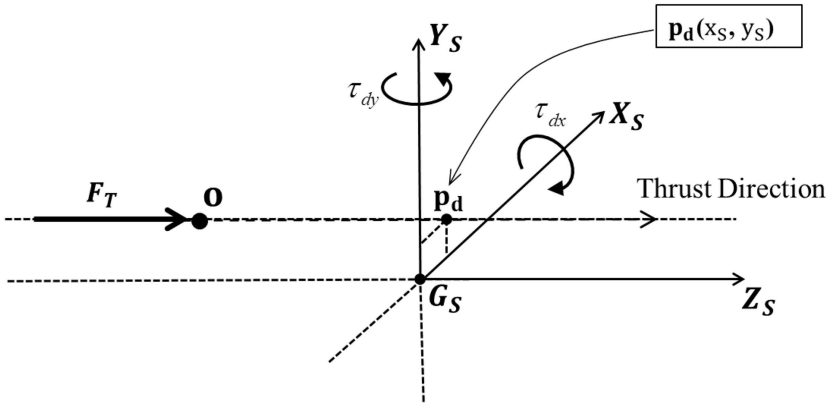

Figure 9. Thrust vector F_T, thrust vector misalignment p_d, and disturbance torques for zero gimbal angle.

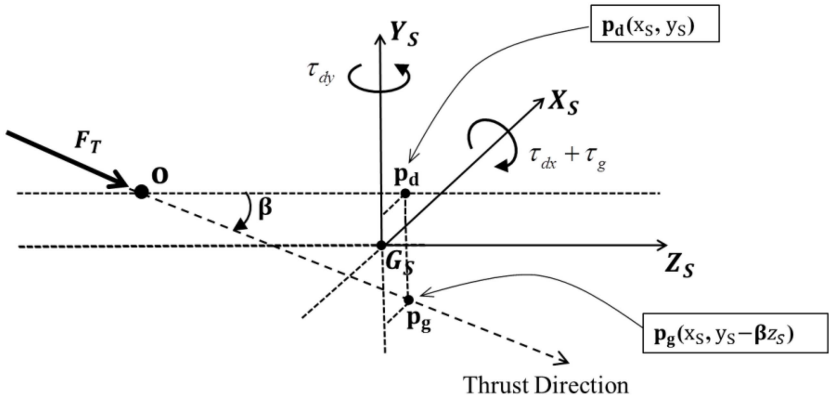

Figure 10. Active control torque τ_g caused by gimbal angle β.

Note that the other orbital disturbance sources such as atmospheric drag, solar pressure, and geomagnetism are so smaller than the disturbance in an impulsive orbital maneuver; therefore, they can be easily neglected.

2.4. State-space model

To simplify the model, similar to [7], some assumptions that are used in this paper are as follows:

$$\sin(\theta)\approx\theta,\qquad \sin(\varphi)\approx\varphi,\qquad \sin(\beta)\approx\beta, \tag{19}$$

$$\mathbf{F}_T^n=\begin{bmatrix}0 & 0 & F_T\end{bmatrix}^T,\qquad \boldsymbol{\rho}_{no}^n=\begin{bmatrix}0 & 0 & z_n\end{bmatrix}^T,$$

$$\boldsymbol{\rho}_{nT}^n=\mathbf{0}_{3\times1},\qquad \boldsymbol{\rho}_{so}=\begin{bmatrix}x_s & y_s & -z_s\end{bmatrix}^T,$$

$$\mathbf{I}_n^n=\mathrm{diag}(I_{n2},I_{n2},I_{n1}),\qquad \mathbf{I}_s=\mathrm{diag}(I_{s2},I_{s2},I_{s1}),$$

$$\boldsymbol{\omega}_s(0)=\begin{bmatrix}0 & 0 & \overline{\omega}_s\end{bmatrix}^T. \tag{20}$$

In Eq. (19), both $\sin(\theta)\approx\theta$ and $\sin(\varphi)\approx\varphi$ indicate that the body attitude deviation becomes small as a result of the closed-loop system performance. In addition, $\sin(\beta)\approx\beta$ shows that during the orbital maneuver, a small gimbal angle is enough for attitude stabilization. The assumptions in Eq. (19) are verified in Section 5.

In Eq. (20), the assumption $\mathbf{F}_T^n=\begin{bmatrix}0 & 0 & F_T\end{bmatrix}^T$ shows that the deviation of the thrust force is zero in the nozzle coordinate frame. Further, the assumption $\boldsymbol{\rho}_{no}^n=\begin{bmatrix}0 & 0 & z_n\end{bmatrix}^T$ confirms that the CM of the nozzle is on its line of symmetry. According to the assumption $\boldsymbol{\rho}_{nT}^n=\mathbf{0}_{3\times1}$, the point of applying the thrust force is coincident with the CM of the nozzle. In $\mathbf{I}_n^n=\mathrm{diag}(I_{n2},I_{n2},I_{n1})$ and $\mathbf{I}_s=\mathrm{diag}(I_{s2},I_{s2},I_{s1})$, the moments of inertia of both body and nozzle are diagonal. Moreover, $\boldsymbol{\omega}_s(0)=\begin{bmatrix}0 & 0 & \overline{\omega}_s\end{bmatrix}^T$ represents the initial condition of the spacecraft body where the two lateral angular velocities are zero and the angular velocity about the longitudinal axis is the spin rate $\overline{\omega}_s$.

The state vector that should be regulated is $\mathbf{X}=\begin{bmatrix}\varphi & \theta & \omega_{sx} & \omega_{sy} & \beta & \dot{\beta}\end{bmatrix}^T$. Of note, $\varphi=\theta=0$ is indicative of the spin-axis stabilization. The linear state-space model can be obtained by substituting the assumptions of Eqs. (19) and (20), as shown in the following:

$$\dot{\mathbf{X}}(t)=\mathbf{A}\mathbf{X}(t)+\mathbf{B}u(t)+\boldsymbol{\Gamma}(t)+\mathbf{D}(t), \tag{21}$$

where:

$$\mathbf{A}=\begin{bmatrix}0 & \overline{\omega}_s & 1 & 0 & 0 & 0\\ -\overline{\omega}_s & 0 & 0 & 1 & 0 & 0\\ 0 & 0 & 0 & -\lambda & -I_\beta & 0\\ 0 & 0 & \lambda & 0 & 0 & I_{nM}\overline{\omega}_s\\ 0 & 0 & 0 & 0 & 0 & 1\\ 0 & 0 & 0 & 0 & 0 & 0\end{bmatrix},$$

$$\mathbf{B}=\begin{bmatrix}0\\0\\-I_r\\0\\0\\1\end{bmatrix},\qquad \mathbf{D}(t)=\begin{bmatrix}0\\0\\\tau_{dx}\\\tau_{dy}\\0\\0\end{bmatrix}\left(\frac{1}{I_2}\right),$$

$$\boldsymbol{\Gamma}(t)=\begin{bmatrix}0\\0\\h_w\overline{\omega}_s\sin(\gamma_x)\\-h_w\overline{\omega}_s\sin(\gamma_y)\\0\\0\end{bmatrix}\left(\frac{1}{I_2}\right).$$

The control input is $\ddot{\beta}=u$, $\mathbf{D}(t)$ includes the disturbances τ_{dx} and τ_{dy}, and $\boldsymbol{\Gamma}(t)$ includes the two CMGs gyroscopic torques ($h_w\overline{\omega}_s\sin(\gamma_x)$ and $-h_w\overline{\omega}_s\sin(\gamma_y)$). The other parameters are:

$$I_1=I_{n1}+I_{s1},\qquad I_2=I_{n2}+I_{s2}+M(z_n+z_s)^2,$$

$$(I_1-I_2)\overline{\omega}_s=I_2\lambda,\qquad I_{n2}+M(z_n+z_s)z_n=I_rI_2,$$

$$I_{n1}-I_{n2}-M(z_n+z_s)z_n=I_{nz}I_2,$$

$$(F_TMz_s)/m_n+I_{nz}I_2\overline{\omega}_s^2=I_\beta I_2,$$

$$I_{nm}=I_{nz}-I_r\Leftrightarrow(I_{n1}-2I_{n2}-2M(z_n+z_s)z_n)=I_{nm}I_2.$$

Note that the torques resulting from the CMG gimbal angular velocity ($\dot{\gamma}_x,\dot{\gamma}_y$) and acceleration ($\ddot{\gamma}_x,\ddot{\gamma}_y$) are neglected in the linearized model compared to the CMGs high-level gyroscopic torques.

3. Control logic

In order to reject the disturbance torques and stabilize the attitude (thrust vector), the control logic is first proposed for gimbal steering of CMG and then, the stability of the closed-loop system is proved using a full-state feedback controller. For disturbance rejection, the two control inputs are $\ddot{\gamma}_x$ and $\ddot{\gamma}_y$ as the CMGs gimbal angular accelerations. The disturbance torques are supposed to be estimated by a disturbance estimator [27,28].

In order to steer each CMG gimbal, a feed-forward controller is considered as follows:

$$\ddot{\gamma}_x=-k_d\dot{\gamma}_x-k_p(\gamma_x-\gamma_{x,d}),$$

$$\ddot{\gamma}_y=-k_d\dot{\gamma}_y-k_p(\gamma_y-\gamma_{y,d}), \tag{22}$$

where k_d and k_p are the positive controller gains and:

$$\gamma_{x,d}=-\sin^{-1}\left(\frac{\tau_{dx}}{h_w\overline{\omega}_s}\right),$$

$$\gamma_{y,d}=\sin^{-1}\left(\frac{\tau_{dy}}{h_w\overline{\omega}_s}\right). \tag{23}$$

If we consider the error $e(t) = \gamma_x - \gamma_{x,d}$, the error dynamics:

$$\ddot{e}(t) + k_d\dot{e}(t) + k_p e(t) = 0, \tag{24}$$

is achieved, which is stable. In addition, k_d and k_p can be obtained using the two parameters ζ and ω_n as:

$$k_d = 2\zeta\omega_n, \qquad k_p = \omega_n^2, \tag{25}$$

where ζ and ω_n are two design parameters to be designed in Section 5.

The following equation is obtained based on Eq. (23):

$$\mathbf{\Gamma}(t) + \mathbf{D}(t) = \left(\frac{h_w\overline{\omega}_s}{I_2}\right)\begin{bmatrix} 0 \\ 0 \\ \sin(\gamma_x) - \sin(\gamma_{x,d}) \\ -\sin(\gamma_y) + \sin(\gamma_{y,d}) \\ 0 \\ 0 \end{bmatrix}$$

$$= \frac{h_w\overline{\omega}_s}{I_2}\mathbf{S}(t). \tag{26}$$

Here, according to control law (Eq. (22)) and error dynamics (Eq. (24)) vector $\mathbf{S}(t)$ is bounded by $\|\mathbf{S}(t)\| \leq \sqrt{2}$ and upon increasing the time, we have $\mathbf{S}(t) \to 0$. Then, the state-space model (Eq. (21)) is reformed into the following:

$$\dot{\mathbf{X}}(t) = \mathbf{A}\mathbf{X}(t) + \mathbf{B}u(t) + \frac{h_w\overline{\omega}_s}{I_2}\mathbf{S}(t). \tag{27}$$

The following full-state feedback controller is considered in activating the 1DoF gimbaled-TVC:

$$u(t) = -\mathbf{K}\mathbf{X}(t). \tag{28}$$

Note that matrix $\tilde{\mathbf{A}} = \mathbf{A} - \mathbf{B}\mathbf{K}$ can be a stable matrix by selecting a proper gain $\mathbf{K}$. Followed by applying Control Input (28) to System (27), the closed-loop system is obtained as:

$$\dot{\mathbf{X}}(t) = \tilde{\mathbf{A}}\mathbf{X}(t) + \frac{h_w\overline{\omega}_s}{I_2}S(t). \tag{29}$$

For an arbitrary positive symmetric matrix $\mathbf{Q} > 0$, we can find a unique positive symmetric matrix $\mathbf{P}$ such that the Lyapunov equation in Eq. (30) is satisfied:

$$\tilde{\mathbf{A}}^T\mathbf{P} + \mathbf{P}\tilde{\mathbf{A}} = -\mathbf{Q}. \tag{30}$$

Consider the following Lyapunov function:

$$V(t) = \mathbf{X}^T(t)\mathbf{P}\mathbf{X}(t).$$

The time derivative of $V(t)$ will be:

$$\dot{V} = \mathbf{X}^T(t)\left[\tilde{\mathbf{A}}^T\mathbf{P} + \mathbf{P}\tilde{\mathbf{A}}\right]\mathbf{X}(t) + 2\mathbf{X}^T(t)\mathbf{P}\frac{h_w\overline{\omega}_s}{I_2}\mathbf{S}(t)$$

$$= -\mathbf{X}^T(t)\mathbf{Q}\mathbf{X}(t) + 2\frac{h_w\overline{\omega}_s}{I_2}\mathbf{X}^T(t)\mathbf{P}\mathbf{S}(t), \tag{31}$$

we have:

$$\mathbf{X}^T(t)\mathbf{Q}\mathbf{X}(t) \geq \lambda_{\min}(\mathbf{Q})\|\mathbf{X}(t)\|^2 \Rightarrow -\mathbf{X}^T(t)\mathbf{Q}\mathbf{X}(t)$$

$$\leq -\lambda_{\min}(\mathbf{Q})\|\mathbf{X}(t)\|^2,$$

$$\left|\mathbf{X}^T(t)\mathbf{P}\mathbf{S}(t)\right| \leq \lambda_{\max}(\mathbf{P})\|\mathbf{X}(t)\|\|\mathbf{S}(t)\|, \tag{32}$$

where $\lambda_{\max}$ and $\lambda_{\min}$ denote the maximum and minimum eigenvalues of a matrix, respectively.

Through Eq. (32), Eq. (31) is reformed into the following:

$$\dot{V} \leq -\|\mathbf{X}(t)\|\left(\lambda_{\min}(\mathbf{Q})\|\mathbf{X}(t)\| - 2\frac{h_w\overline{\omega}_s}{I_2}\lambda_{\max}(\mathbf{P})\|\mathbf{S}(t)\|\right). \tag{33}$$

As mentioned earlier, while increasing time, we have $\mathbf{S}(t) \to 0$ and $\lambda_{\min}(\mathbf{Q}) > 0$; thus, we have:

$$\dot{V} < 0 \Rightarrow \mathbf{X}(t) \to 0 \quad \text{as} \quad t \to \infty,$$

pointing to the stability of the closed-loop system.

4. Spacecraft parameters

In this section, the spacecraft and orbital mission parameters are determined. Orbiting Frog Otolith (OFO) spacecraft, which was launched in 1970, was 132 kg in weight mass and 1.7×0.8 m in dimensions. Spacecraft body and nozzle length were selected as 1.5 m ($z_s = 0.75$ m) and 0.4 m ($z_n = 0.2$ m), respectively, and the spacecraft body width was 1 m.

The velocity changes for the orbital maneuver of the space shuttle, Mercury, Gemini, Soyuz were 90 m/s, 168 m/s, 98 m/s, and 115 m/s, respectively. For an atmospheric reentry from the altitude of 400 km, the velocity change of 100 m/s was enough [29]. In this research, $\Delta v_d = 100$ m/s was selected for an impulsive orbital maneuver.

For an orbit with an altitude higher than 250 km, the orbit period T_{Orb} was more than 90 min. In this paper, the burning time was measured as $T_b = 50$ s, thus satisfying the condition $T_b/T_{\text{Orb}} << 0.01$ for an impulsive orbital maneuver.

The following calculations give the solid fuel mass for the SRM:

$$\dot{m}_f = \frac{F_T}{gI_{sp}},$$

$$F_T = (m_n + m_s)\frac{\Delta V_d}{T_b} \approx m_s \frac{\Delta V_d}{T_b} \Rightarrow \dot{m}_f \approx \frac{m_s \Delta V_d}{gI_{sp}T_b},$$

$$m_f \approx \dot{m}_f T_b = \frac{m_s \Delta V_d}{gI_{sp}} = \frac{150 \times 100}{10 \times 260} = 5.8 \text{ kg},$$

where $\dot{m}_f$ is the fuel consumption rate, F_T the thrust force, $I_{sp} = 260$ s the fuel-specific impulse, and $m_f = 5.8$ kg the fuel mass. Finally, the mass of nozzle including m_f is $m_n = 8$ kg.

The moment of inertia depends on the mass distribution. The transverse moment of inertia for the spacecraft body was estimated as $I_{xx,s} = I_{yy,s} = I_{s2} \approx 10$ kgm^2, and the moment of inertia about the z_s axis (I_{s1}) was supposed to be as a design variable (for $I_{s1} > 1$ and $I_{s1} < 1$, the body contains a disc and a cylindrical shape, respectively). The moment of inertia of the nozzle was estimated as $I_{xx,n} = I_{yy,n} = I_{n2} = 1$ kgm^2 and $I_{zz,n} = I_{n1} = 0.5$ kgm^2.

The wheel speed of the CMG could reach 40000 rpm [30]; however, the smaller value was considered here, i.e., $\omega_g = 750$ rad/s (7161 rpm).

The parameters of the spacecraft and controller used in the controller design and simulations are listed in Table 1. The maximum acceleration and thrust force were calculated as $a_{\max} = 2$ m/s^2 and $F_T = (m_n + m_s)a_{\max} = 316$ N, respectively. The value of J_d was calculated from each CMG mass $m_g = 2$ kg and radius $r = 0.1$ m through the following formula:

$$J_d = m_g r^2/2.$$

Given that this study considered a small spacecraft, a 1DoF gimbaled-TVC was used instead of a 2DoF one. Through this selection, an effective control input is inactivated and consequently, the control problem becomes more complicated.

5. Control system design

In addition to the control gain $\mathbf{K}$, the other two important parameters associated with the closed-loop control system are $\overline{\omega}_s$ and I_{s1}. This section primarily aims to design the closed-loop system parameters $\overline{\omega}_s$, I_{s1}, and $\mathbf{K}$. Given the significance of the disturbance rejection as an important task of the closed-loop system, high-level disturbances of $\tau_{dx} = 25$ Nm and $\tau_{dy} = 25$ Nm were taken into account which were equivalent to the CM offset of $y_s = 8.3$ cm and $x_s = -8.3$ cm (from Eq. (18)). In [7], a closed-loop system was designed for maximum 4 Nm disturbance, which is smaller than the disturbance considered in this paper. In fact, there are infinity parameters to stabilize the closed-loop system. Table 2 lists the eight obtained control systems through the trial-and-error method. Note that the maximum disturbance, which can be rejected by each CMG, is calculated through $\tau_{d,\max} = h_w\overline{\omega}_s = J_d\omega_g\overline{\omega}_s$. The other required parameters are listed in Table 1. All $\tau_{d,\max}$'s are bigger than the disturbance torque level applied to the spacecraft.

In Eq. (25), ζ and ω_n are the two parameters related to the steering logic of the CMG that should be designed. In this regard, the relation between t_s as the settling time of CMG gimbal and ζ and ω_n can be written as follows:

$$\omega_n \approx \frac{4}{\zeta t_s}. \tag{34}$$

The smaller the t_s, the faster the disturbance rejection. In the case of choosing smaller t_s value, the

Table 1. Spacecraft and orbital mission parameters.

T_b	Δv_d	ω_g	J_d	I_{s2}	I_{n2}	I_{n1}	m_s	m_n	Z_n	Z_s
50	100	750	0.01	10	1	0.5	150	8	0.2	0.75

Table 2. Eight control systems parameters.

Control system	$\overline{\omega}_s$	I_{s1}	$\tau_{d,\max}$	K
1	4	12	30	[−15.86 −67.77 −51.23 10.26 166.65 12.18]
2	3.5	23.99	26.25	[18.92 −23.42 −9.35 −1.96 59.08 10.37]
3	4	24.5	30	[26.55 −70.00 −21.97 2.53 101.50 11.69]
4	4.5	24.191	33.75	[22.34 −125.54 −45.51 2.34 143.68 11.36]
5	4.8	25.542	36	[81.38 −126.48 −25.19 7.64 137.67 12.84]
6	5.5	19.335	110	[102.02 −20.45 −13.99 −24.94 72.59 13.27]
7	6	18.944	45	[143.45 −24.75 −17.40 −35.11 75.11 13.97]
8	5.5	25.946	110	[188.83 −249.40 −43.40 20.83 231.19 14.71]

gimbal angle of the CMG converges to its desired values $(\gamma_{x,d}, \gamma_{y,d})$ faster. Moreover, t_s affects the maximum overshoot of spacecraft state variables $\mathbf{X}$. To evaluate the performance and advantages of the eight controllers in the range of $0.5s \leq t_s \leq 25s$, three main outputs were obtained: maximum gimbal angle (β_m), maximum thrust vector deviation (δ_{FT}), and velocity change (Δv_z). In addition, the effect of disturbance rejection speed on the system performance was evaluated.

In the following, the eight controllers in Table 2 are used to determine the values of β_m, $\delta_{FT,\max}$, and Δv_z in the range of $0.5s \leq t_s \leq 25s$. For the gimbal controller of the CMG, the value of $\zeta = 0.8$ is considered as a constant.

Given that $\delta_{FT}(t) = \cos^{-1}(\cos(\theta(t))\cos(\varphi(t) + \beta(t)))$, the value of $\delta_{FT,\max}$ approximately shows the maximum overshoot of $\theta(t)$ and $\varphi(t)$. Therefore, the validity of the assumptions in Eq. (19) can be checked using the following results.

Figures 11–14 show the values of β_m versus t_s for some control systems. Figures 15–18 present the values of $\delta_{FT,\max}$ and Δv_z versus t_s.

Following a comparative analysis, a good controller is found as the one that satisfies the assumptions in Eq. (19) and results in a bigger Δv_z. Although some controllers cannot satisfy the assumptions in Eq. (19), they can stabilize the spacecraft attitude

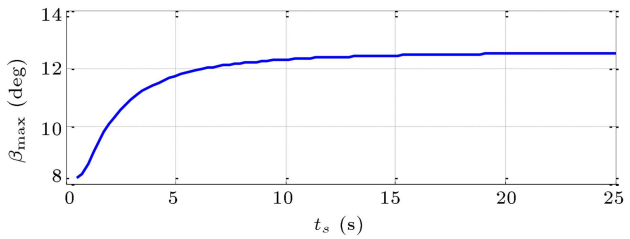

Figure 11. Maximum gimbal angle versus the CMG settling time for the control system (1).

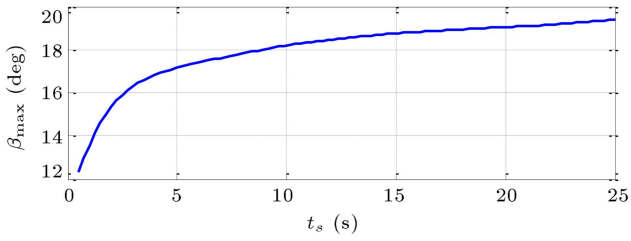

Figure 12. Maximum gimbal angle versus the CMG settling time for the control system (3).

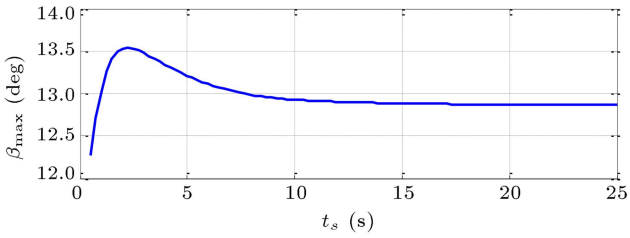

Figure 13. Maximum gimbal angle versus the CMG settling time for the control system (4).

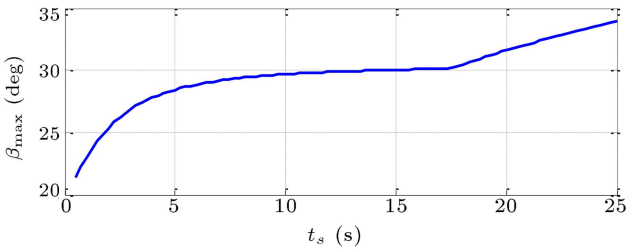

Figure 14. Maximum gimbal angle versus the CMG settling time for the control system (5).

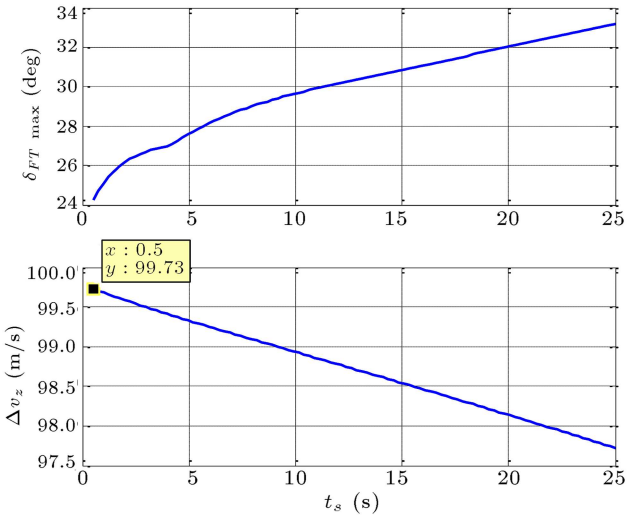

Figure 15. Maximum thrust vector deviation (δ_{FT}) and velocity change (Δv_z) versus the CMG settling time for the control system (1).

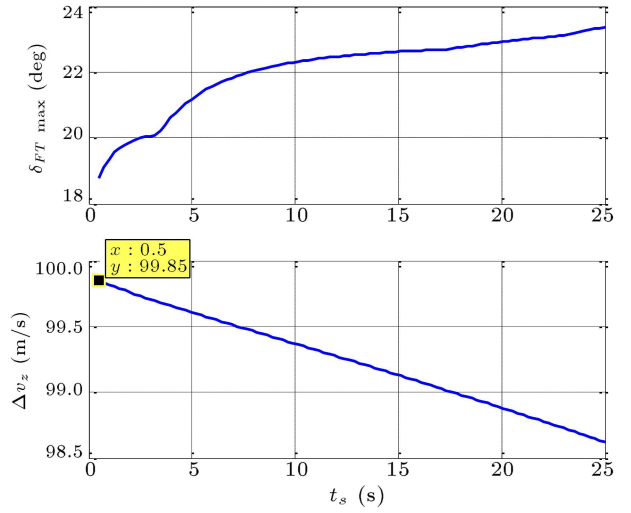

Figure 16. Maximum thrust vector deviation (δ_{FT}) and velocity change (Δv_z) versus the CMG settling time for the control system (3).

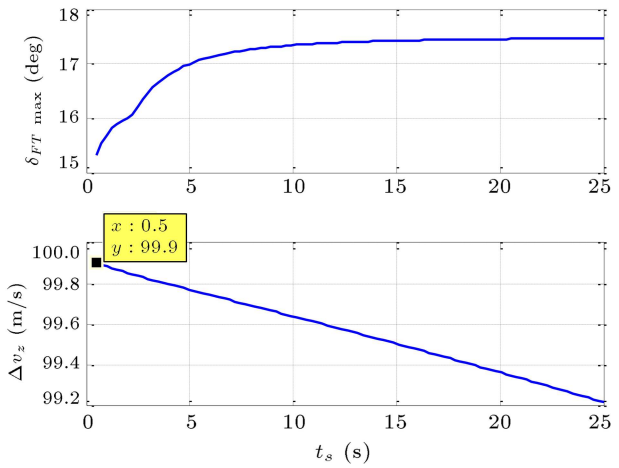

Figure 17. Maximum thrust vector deviation (δ_{FT}) and velocity change (Δv_z) versus the CMG settling time for the control system (4).

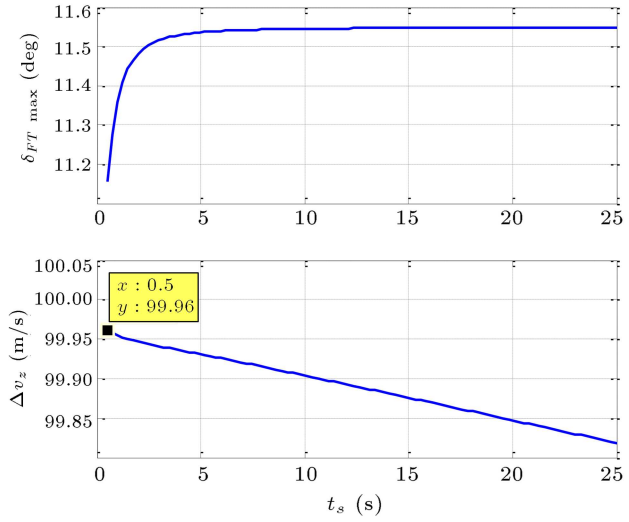

Figure 18. Maximum thrust vector deviation (δ_{FT}) and velocity change (Δv_z) versus the CMG settling time for the control system (5).

during the numerical simulation. The assumptions in Eq. (19) are used for linearization of the nonlinear model; the violation of these assumption does not mean the instability of the closed-loop system (the closed-loop system includes the linear controller and nonlinear plant). It is better for a controller to satisfy the assumptions in Eq. (19).

The important findings of this numerical analysis are listed below:

1. In the control systems 1, 2, 3, 4, 6, and 7, upon increasing the t_s from 0.5 s to 5 s, the value of β_m will increase; however, for $5s \leq t_s \leq 25s$, β_m remains approximately constant. Increasing t_s in control systems 5 and 8 always results in an increase in β_m;
2. Increasing t_s in all control systems always results in a decrease in Δv_z. A straight-line equation can describe the relation between Δv_z and t_s. Therefore, it can be concluded that the faster the disturbance rejection, the higher the Δv_z value and the more accurate the orbital maneuver ($\Delta v_d = 100$ m/s). Although smaller t_s values yield better Δv_z, the assumptions in Eq. (19) should still be satisfied; therefore, β_m and $\delta_{FT,\max}$ should be investigated for each controller;
3. The maximum Δv_z values in these eight controllers are 5(99.96 m/s), 8(99.95 m/s), 4(99.90 m/s), 3(99.85 m/s), 1(99.73 m/s), 2(99.70 m/s), 6(99.63 m/s), and 7(99.63 m/s). For each control system, the maximum Δv_z is achieved for the smallest $t_s = 0.5$ s;
4. In all of these controllers, the smallest $t_s = 0.5$ s results in the smallest β_m and $\delta_{FT,\max}$. However, the control system 4 is the best among the others in satisfying the assumptions in Eq. (19). In addition, it generates a reasonable Δv_z (99.90 m/s), which is more accurate than controllers 1, 2, 3, 6, and 7;
5. Although the control system 5 has the best Δv_z (99.96 m/s), it does not function better than controller 4 in satisfying the assumptions in Eq. (19);
6. Obviously, upon decreasing the CM offset (smaller disturbance), better Δv_z is achieved;
7. In addition to gain $\mathbf{K}$, the two parameters $\overline{\omega}_s$ and I_{s1} play an important role in the functionality of the closed-loop system by which a designer is able to design an efficient and accurate control system;
8. Fast disturbance rejection (smaller t_s) is suitable for both obtaining an accurate Δv_z and satisfying the assumptions in Eq. (19).

Note that there are infinity control systems, among the eight of which the control system 4 was selected as the best controller. It is likely that someone can find a better control system in the future.

6. Simulation results

The main objectives of the simulation are to show the effectiveness of the CMGs in rejecting the large disturbance torques and stabilizing the spin-axis (thrust vector). Simulations were done based on the data presented in Table 1, controller 4 in Table 2, and $t_s = 0.5$ s. Although the linearized model was used for controller design, the linear controller was applied to the nonlinear system in the all simulations to demonstrate the applicability of the proposed method.

The spacecraft body attitude (φ, θ) and thrust vector deviation (δ_{FT}) are shown in Figure 19 where δ_{FT} is fully regulated with the maximum deviation of $\delta_{FT,m} = 15.3°$. The maximum overshots for the body

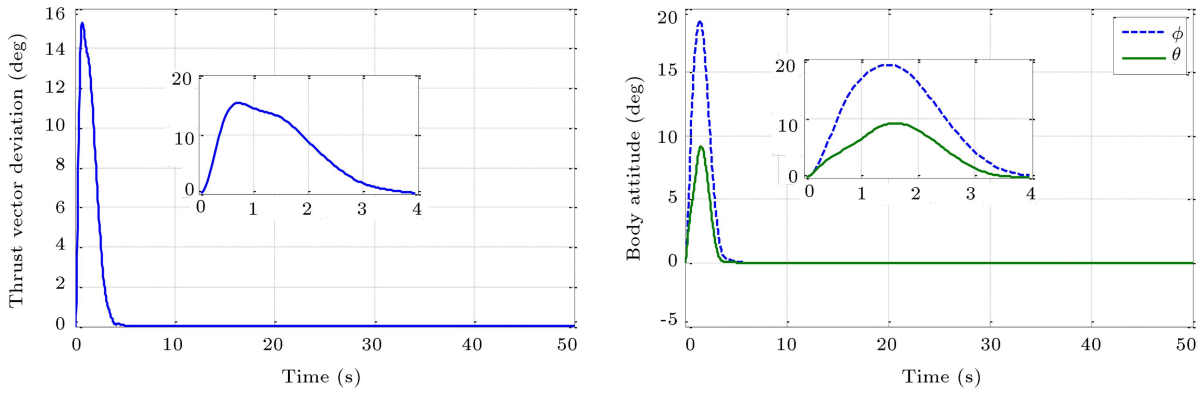

Figure 19. Attitude (φ, θ) and thrust vector deviation (δ_{FT}).

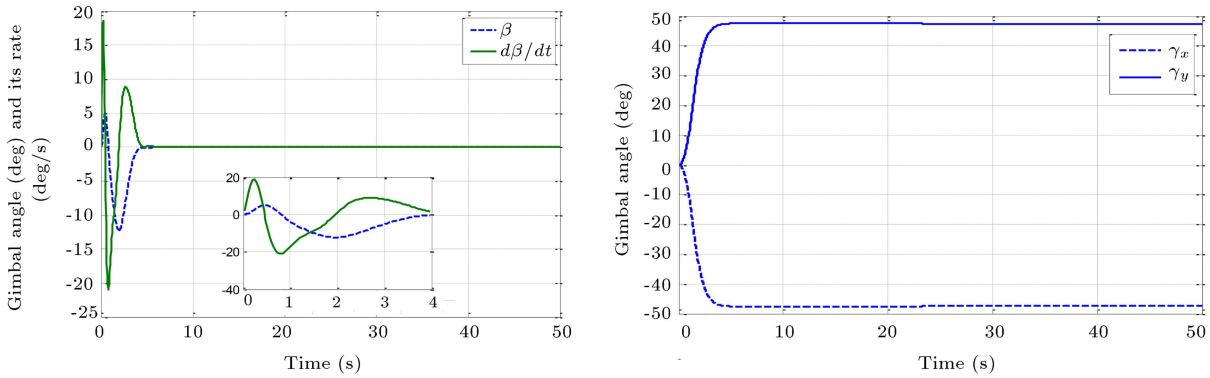

Figure 20. Nozzle gimbal angle and its rate (β, $\dot{\beta}$) and the gimbal angle of the two CMGs.

attitude are $\varphi_m = 19°$ and $\theta_m = 9.2°$ that satisfy the two assumptions in Eq. (19). First, the disturbance torques cause a large attitude deviation and then, with an increase in time, the disturbance torques are fully rejected by the gyroscopic torques of the two CMGs.

In addition, ω_{sx} and ω_{sy} as the spacecraft body angular velocities are completely eliminated with the overshoots $\omega_{sx,m} = 49.7$ and $\omega_{sx,m} = 93$ (deg/s). In comparison with $\Delta v_d = 100$ m/s, an accurate velocity change Δv_z is calculated as 99.90 m/s.

The control input $u = \ddot{\beta}$, gimbal angle β and its rate $\dot{\beta}$ are given in Figure 20. The maximum deflection of the gimbal angle is 12.26 deg, which satisfies the third assumption in Eq. (19). As shown in Figure 20, the gimbal angles (γ_x, γ_y) of the CMG are activated very fast to reject the disturbances quickly. The interaction between the spacecraft spin rate $\overline{\omega}_s$ and CMGs angular momentum h_w is proved to be useful for rejecting the disturbance torques.

The important limitations of the proposed control method are listed below:

1. Using a CMG instead of an RW may increases the complexity of the control system;
2. When the spacecraft has flexible links, using spin stabilization is not suitable for attitude control.

The innovations of this paper are summarized as follows:

1. This method is suitable for impulsive orbital maneuvers with short burning time and high-level disturbance;
2. In this method, the thrust vector stabilization is very fast through which a large velocity change can be obtained;
3. The disturbance level, which is rejected by this method, is larger than that of previous works;
4. The disturbance rejection is done without using the RCSs that use liquid fuel;
5. In comparison to RW, a CMG with a smaller weight can store much more angular momentum;
6. In addition to the above-mentioned advantages, the proposed method also enjoys the advantages of the research [7].

7. Conclusion

The present study proposed a method to develop an efficient and implementable control system for small spacecrafts without using Reaction Control System (RCS). For simplicity, this method was designed in a

way that could operate with a one Degree of Freedom (1DoF) gimbaled-TVC (instead of 2DoF) and two small Control Moment Gyroses (CMGs).

In an impulsive orbital maneuver, a large disturbance torque was generated and the burning time was too short. In this regard, the main objective of this study was to reject the large disturbance torque very quickly. Since a large angular momentum was generated in each wheel of the CMG, a large control torque was produced to reject large disturbances. Since each CMG was gimbaled to the spacecraft body, its angular momentum direction was changed easily and very fast, thus making the control torque reject the disturbance quickly.

Numerical simulations revealed that all state variables (including thrust vector deviation) converged to zero despite the presence of disturbance torques. The results demonstrated that the faster the disturbance rejection, the better the velocity change. The closed-loop control system was designed for the maximum disturbance level. Obviously, smaller disturbances resulted in better velocity change. In addition to the disturbance effect, it could eliminate the initial attitude deviation easily.

Since there was enough time for speeding up the CMG wheel before the thrusting maneuver, a large angular momentum was stored in each CMG while the axial torque of each CMG was very small. In this respect, only electrical power was required to store a large angular momentum.

In case a spacecraft needs two Reaction Wheels (RWs), two RWs can be easily obtained by setting the two CMGs gimbal angles to 90°. Therefore, these wheels can be used for attitude control at non-thrusting phases such as pointing the spacecraft antenna toward the earth.

For future research, the author aims to extend the proposed method for thrusting maneuvers of a flexible spacecraft.

Nomenclature

m_n	Nozzle mass (kg)
$\mathbf{K}$	Linear controller gain
F_T	Thrust force (N)
G_n	Nozzle CM location
G_s	Body CM location
Δv_d	Desired velocity change (m/s)
$x_s y_s z_s$	Body-fixed coordinate frame
$\Delta \mathbf{v}$	Velocity change increment (m/s)
$\mathbf{F}_o$	Interaction force at the pivot o (N)
h_w	The CMG angular momentum (Nms)
J_d	The gimbal wheel axial moment of inertia (kgm^2)
Δv_z	Velocity change in Z_I direction (m/s)
T_{Orb}	The orbit period (s)
I_{sp}	The fuel specific impulse (s)
m_s	Body mass (kg)
u	Control input (rad/s^2)
I_{n2}	Nozzle moment of inertia (kgm^2)
I_{s2}	Body moment of inertia (kgm^2)
T_b	Burning time (s)
$X_I Y_I Z_I$	Inertial coordinate system
$x_n y_n z_n$	Nozzle-fixed coordinate frame
$\mathbf{M}_o$	Interaction torque at the pivot o (Nm)
t_s	Settling time of CMG's gimbal (s)
z_n	The distance of the pivot o from the CMs of the nozzle (m)
z_s	The distance of the pivot o from the CMs of the body (m)
x_s, y_s	The CM offset or thrust vector misalignment (m)
$\dot{m}_f$	The fuel consumption rate (kg/s)
m_f	The fuel mass (kg)

Greek symbols

β	Gimbal rotation angle (rad)
θ	Body attitude angle (rad)
$\boldsymbol{\tau}_s$	Body external torque (Nm)
$\boldsymbol{\tau}_n$	Nozzle external torque (Nm)
$\boldsymbol{\tau}_d$	Exogenous disturbance (Nm)
$\boldsymbol{\omega}_n$	Nozzle angular velocity (rad/s)
γ_x	The gimbal angle around x_s (rad)
ω_g	The gimbal wheel spin rate (rad/s)
$\overline{\omega}_s$	Spacecraft spin rate (rad/s)
δ_{FT}	Thrust vector deviation from the Z_I (rad)
$\dot{\boldsymbol{\omega}}_r$	Angular acceleration of the nozzle with respect to the body (rad/s^2)
$\boldsymbol{\omega}_r$	Angular velocity of the nozzle with respect to the body (rad/s)
$\dot{\omega}_s$	Spacecraft body angular acceleration (rad/s^2)
$\boldsymbol{\omega}_s$	Body angular velocity (rad/s)
γ_y	The gimbal angle around y_s (rad)
φ, θ, ψ	Euler angles of the body with respect to the inertial coordinate (rad)
$\tau_{d,\max}$	the maximum disturbance can be rejected by each CMG (Nm)

Subscripts

s	The body
n	The nozzle
o	Gimbal pivot
T	The point of acting the thrust force

References

1. Saberi, F.F., Kabganian, M., Kouhi, H., et al. "Gimbaled-thruster based nonlinear attitude control of a small spacecraft during thrusting manoeuvre", *The Aeronautical Journal*, **121**(1241), p. 983 (2017).
2. Liu, X., Xin, X., Li, Z., et al. "Parameter identification-based attitude stabilization control of spacecraft with multiaccessories during orbital maneuver", *Journal of Aerospace Engineering*, **30**(3), p. 04016099 (2017).
3. Toloei, A. and Asgari, H. "Quaternion-based finite-time sliding mode controller design for attitude tracking of a rigid spacecraft during high-thrust orbital maneuver in the presence of disturbance torques", *International Journal of Engineering*, **32**(3), pp. 430–437 (2019).
4. Morales, J.E., Kim, J., and Richardson, R.R. "Gyroless spin-stabilization controller and deorbiting algorithm for cubesats", *International Journal of Aeronautical and Space Sciences*, **22**, pp. 445–455 (2021). https://doi.org/10.1007/s42405-020-00311-5
5. Mishne, D. "Orbital maneuvers of nanosatellites using electrical micro-propulsion system, with drag augmentation", The 60th Israel Annual Conference on Aerospace Sciences, 2020At: Tel-Aviv & Haifa, Israel, March 4–5 (2020).
6. Noll, R., *Spacecraft Attitude Control During Thrusting Maneuvers*, NASA SP-8059 (1971).
7. Kouhi, H., Kabganian, M., Saberi, F.F., et al. "Robust control of a spin-stabilized spacecraft via a 1DoF gimbaled-thruster and two reaction wheels", *ISA Transactions*, **66**, pp. 310–324 (2017).
8. Thienel, J.K. and Markley, F.L. "Comparison of angular velocity estimation methods for spinning spacecraft, in advances in astronautical science", *AAS/AIAA Guidance, Navigation, and Control Conference* (2011).
9. Martin, K.M. and Longuski, J.M. "Velocity pointing error reduction for spinning, thrusting spacecraft via heuristic thrust profiles", *Journal of Spacecraft and Rockets*, **52**(4), pp. 1268–1272 (2015).
10. Gui, H. and Vukovich, G. "Robust adaptive spin-axis stabilization of a symmetric spacecraft using two bounded torques", *Advances in Space Research*, **56**(11), pp. 2495–2507 (2015).
11. Yaghoubi, D. and Schnell, A. "Mars ascent vehicle solid propulsion configuration", In *2020 IEEE Aerospace Conference* IEEE (2020).
12. Reyhanoglu, M. and Hervas, J.R. "Nonlinear dynamics and control of space vehicles with multiple fuel slosh modes", *Control Engineering Practice*, **20**(9), pp. 912–918 (2012).
13. Gui, H., Sun, R., Chen, W., et al. "Reaction control system optimization for maneuverable reentry vehicles based on particle swarm optimization", *Discrete Dynamics in Nature and Society*, **2020** (2020). https://www.hindawi.com/journals/ddns/2020/6518531/
14. Yeh, F.-K. "Sliding-mode-based contour-following controller for guidance and autopilot systems of launch vehicles", *Proceedings of the Institution of Mechanical Engineers, Part G: Journal of Aerospace Engineering*, **227**(2), pp. 285–302 (2013).
15. Wang, Z., Jia, Y., Jin, L., et al. "Thrust vector control of upper stage with a gimbaled thruster during orbit transfer", *Acta Astronautica*, **127**, pp. 359–366 (2016).
16. Shi, C., Yang, J., and Xu, Z. "Research on thrust vector control of nonlinear solid rocket motor nozzle based on active disturbance rejection technology". In *MATEC Web of Conferences, EDP Sciences* (2020).
17. Rizvi, F. and Weitl, R.M. "Characterizing limit cycles in the cassini thrust vector control system", *Journal of Guidance, Control, and Dynamics*, **36**(5), pp. 1490–1500 (2013).
18. Felicetti, L., Sabatini, M., Pisculli, A., et al. "Adaptive thrust vector control during on-orbit servicing", In *Proceedings of AIAA SPACE 2014 Conference and Exposition*, paper AIAA-2014-4341, San Diego (2014).
19. Kouhi, H., Kabganian, M., Shahravi, M., et al. "Retrofiring control method via combination of a 1DoF gimbaled thrust vector control and spin-stabilization", *Proceedings of the Institution of Mechanical Engineers, Part G: Journal of Aerospace Engineering*, **231**(7), pp. 1199–1212 (2017).
20. Bagheri, M., Kabganian, M., and Nadafi, R. "Three-axis attitude control design for a spacecraft based on Lyapunov stability criteria", *Scientia Iranica*, **20**(4), pp. 1302–1309 (2013).
21. Wu, Y., Han, F., Zheng, M., et al. "Attitude control for on-orbit servicing spacecraft using hybrid actuator", *Advances in Space Research*, **61**(6), pp. 1600–1616 (2018).
22. Wu, Y.-H., Han, F., Zhang, S.-J., et al. "Attitude agile maneuvering control for spacecraft equipped with hybrid actuators", *Journal of Guidance, Control, and Dynamics*, **41**(3), pp. 809–812 (2018).
23. Yang, G., Wang, H., Chen, J., et al. "Command filtered robust control of nonlinear systems with full-state time-varying constraints and disturbances rejection", *Nonlinear Dynamics*, **101**(4), pp. 2325–2342 (2020).
24. Kabganian, M., Kouhi, H., Shahravi, M., et al. "Thrusting maneuver control of a small spacecraft via only gimbaled-thruster scheme", *Advances in Space Research*, **61**(9), pp. 2328–2343 (2018).

25. Kouhi, H., Kabganian, M., Fani Saberi, F., et al. "Adaptive control of a spin-stabilized spacecraft using two reaction wheels and a 1DoF gimbaled-thruster", *AUT Journal of Modeling and Simulation*, **49**(1), pp. 103–112 (2017).

26. Kishore, W.A., Dasgupta, S., Ray, G., et al. "Control allocation for an over-actuated Satellite Launch Vehicle", *Aerospace Science and Technology*, **28**(1), pp. 56–71 (2013).

27. Chen, W.-H. "Nonlinear disturbance observer-enhanced dynamic inversion control of missiles", *Journal of Guidance, Control, and Dynamics*, **26**(1), pp. 161–166 (2003).

28. Mobayen, S. and Tchier, F. "Nonsingular fast terminal sliding-mode stabilizer for a class of uncertain nonlinear systems based on disturbance observer", *Scientia Iranica*, **24**(3), pp. 1410–1418 (2017).

29. Burkhardt, H., Sippel, M., Krülle, G., et al. "Evaluation of propulsion systems for satellite end of life de-orbiting", *AIAA Journal*, **4208**, p. 2002 (2002).

30. Yoon, H. and Tsiotras, P. "Spacecraft adaptive attitude and power tracking with variable speed control moment gyroscopes", *Journal of Guidance, Control, and Dynamics*, **25**(6), pp. 1081–1090 (2002).

Biography

Hamed Kouhi is currently a Faculty Member at the Department of Mechanical Engineering at the University of Guilan (Iran). He received his PhD in Mechanical Engineering from Amirkabir University of Technology (Iran) and MSc in Mechanical Engineering from Sharif University of Technology (Iran). He received his BSc in Mechanical Engineering from the University of Guilan in 2008. His specializations are Dynamics, Control, and Navigation.